

See discussions, stats, and author profiles for this publication at: <https://www.researchgate.net/publication/301390100>

# Towards a Highly Efficient Small Scale Turboshaft Engine: Part I — Engine Concept and Compressor Design

Conference Paper · June 2014

DOI: 10.1115/GT2014-26368

---

CITATIONS

2

READS

2,220

4 authors, including:



Ulrich Siller

AeroDesignWorks GmbH, Cologne, Germany

18 PUBLICATIONS 226 CITATIONS

[SEE PROFILE](#)



Tim Moser

Electra.aero

2 PUBLICATIONS 6 CITATIONS

[SEE PROFILE](#)

**GT2014-26368**

## **TOWARDS A HIGHLY EFFICIENT SMALL SCALE TURBOSHAFT ENGINE. PART I: ENGINE CONCEPT AND COMPRESSOR DESIGN.**

**G. Kröger, U. Siller**  
AeroDesignWorks GmbH  
Hauptstraße 108  
50996 Cologne, Germany  
georg.kroeger@aerodesignworks.com  
ulrich.siller@aerodesignworks.com

**T. Moser, S. Hediger**  
Creative Technologies GmbH  
Bachmatten 2a  
4435 Niederndorf, Switzerland  
tim.moser@ctechnologies.ch  
stani.hediger@ctechnologies.ch

### **ABSTRACT**

Today's UAV helicopter industry faces a lack of highly reliable, SFC optimized turboshaft engines in the 40kW to 100kW class, resulting in a significant drawback for the overall flight envelope and the system availability of these aircraft. This paper describes the design process for a turboshaft engine with a shaft power output of about 80kW. A thermodynamic cycle model is derived from the flight envelope of the Swiss UAV NEO S-350 helicopter drone. Different compressor configurations are analysed and discussed with regard to the power output and SFC of the engine as well as to manufacturing constraints. Combining a high flow density with a high isentropic efficiency and pressure ratio, a three stage compressor configuration was selected. The design is based on two axial front stages with a total pressure ratio of 1.55 and 1.45, respectively, and a diagonal last stage with a total pressure ratio of 2.8. Finally, the aero-mechanical design and optimization process of the compressor is depicted and the manufacturing process is described. The engine prototype is expected to be tested the first time in 2014.

### **NOMENCLATURE**

HPT	High pressure turbine
MTOW	Maximum take-off weight
NS	Near stall operating point at design speed
OP	Operating point
PT	Power turbine
RPM	Revolutions per minute [1/min]

SFC	Specific fuel consumption [kg/kW*h]
SM	Surge margin
UAV	Unmanned air vehicle
WL	Working line operating point at design speed

### **INTRODUCTION**

Most of the today's helicopter UAV systems are small, light weight aircraft with a MTOW between 20kg and 300kg. To assure safe operation up to altitudes of about 6000m and aerodynamic stability for agile in-flight maneuverability the required power level ranges from 20kW to about 100kW. Different absolute power requirements aside, the UAVs basically do face the same challenging flight envelope needs as their manned counterparts: Enhanced long endurance properties, low SFC, multi-purpose mission ability, high dispatch reliability and a well balanced maneuverability.

Currently available engines in the given power range are mostly derivates from turboshaft engines for model airplanes or from small scale piston engines. Whereas the turboshaft engines for the model airplanes mainly suffer from a high SFC and substantial quality issues, the piston engines can provide very suitable SFC values at the cost of a lower power-weight ratio and serious engine vibrations. Hence, to achieve the flight envelope goals, highly reliable and SFC optimized turboshaft engines are to be developed.

The first part of this paper outlines the pathway from the customer-defined helicopter operating points to a turboshaft

engine concept. Basic thermodynamic considerations are presented and discussed. A two-shaft engine concept has been selected. Using estimated turbine and burner efficiencies, different compressor concepts are developed and compared with respect to the total pressure ratio and isentropic efficiency of the compressor, engine SFC, compressor integration feasibility and overall engine diameter. Finally, a 3 stage axial-axial-diagonal compressor concept is chosen.

The second part of this paper is dedicated to the compressor aerodynamics. The compressor design is achieved by conventional 2D preliminary design (S2) and automated 3D CFD optimization. A conventional 2D blade-to-blade (S1) airfoil section optimization was not used in this scope. A detailed overview of the compressor aerodynamics is given, including all relevant stage and engine performance data sets. A critical assessment discusses the potential for further improvement in aerodynamic performance. Finally, the mechanical blade design is reviewed in terms the analysis of the static blade stresses and the vibrational modes of the blade.

## BASIC AIRCRAFT DESIGN DATA

The basic design specification for the all new turbo-shaft engine mainly consisted of the helicopter operating points and some assumptions regarding the basic engine design parameters. The MTOW of the helicopter was given as 275kg. The helicopter's main rotor runs at a speed of 850 RPM leading to a power turbine (PT) speed of 85.000 RPM. The use of MAR-M247 as material for the high pressure turbine stage (HPT) prescribes a maximum turbine inlet temperature of 1100K for a completely uncooled turbine configuration.

Table 1 presents the derived operating points (OP) of the Swiss UAV NEO S-350 helicopter drone with the all new engine. The compressor aero-speed refers to the aerodynamic speed variation due to ISA temperature and density effects. Three baseline sea level operating points are defined, namely Hover, Cruise and the Maximum Power point. The most challenging hover conditions at higher altitudes are furthermore specified with a "hover in ground effect (HIGE)" operating point at 4500m and a "hover out of ground effect (HOGE)" operating point at a height of 3250m. The maximum flight height condition is defined with the Maximum Altitude operating point and the maximum rate of climb is to be realized up to an altitude of 4000m the latter being the most challenging operating condition.

## BASIC ENGINE DIMENSIONS

The basic engine diameter of a micro gas turbine for aircraft applications is mainly dictated by the compressor concept. Nearly all known micro turbines use a single stage radial compressor engine layout together with a single stage radial or axial turbine. This engine configuration provides a relatively simple engine setup leading to a compact axial design but,

OP	Power [kW]	ISA Height [m]	Relative reduced speed
Hover	31-35	0	1.000
Cruise	25-28	0	1.000
Max. Power	45	0	1.000
HIGE	31	4500	1.055
HOGE	35	3250	1.039
Max. Altitude	25-28	6000	1.075
Max. Climb	40	4000	1.048

**TABLE 1.** Derived operating points from Swiss UAV Neo S-350 for the new engine

on the other hand, to an increased overall outer diameter due to the radial compressor. Outer diameters of about 100mm are commonly used with a rotating speed of about 100 000 RPM. The drawback of this engine layout is the rather large engine diameter leading to serious issues in relation to engine integration and aerodynamic drag, especially in the case of scaling the engine. A typical micro turbine engine layout is shown in figure 1.

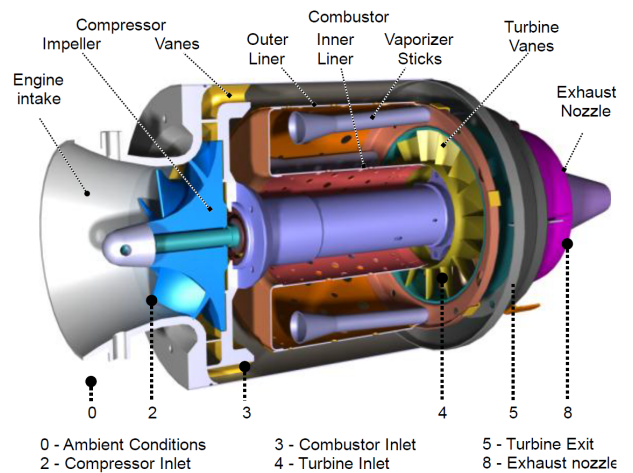


**FIGURE 1.** Typical micro gas turbine engine concept with a single stage radial compressor and a single stage axial turbine [1]

## THERMODYNAMIC CONSIDERATIONS

The thermodynamic considerations regarding the new engine layout are basically determined by the maximum engine diameter, the turbine inlet temperature and the achievable turbo component efficiencies. The employed materials and engine diameter limit the maximum tip speed of the compressor and

the turbine and thus the maximum loading of the components. The turbine inlet temperature defines the overall thermodynamic cycle efficiency of the engine. Finally, the achievable component efficiencies of the compressor and the turbine at design loading conditions define the SFC of the engine presuming the burner efficiency and total pressure loss are known. No accurate estimates of the latter are available for engines of this size that utilize part of the engine fuel for the turbine bearing cooling. Approximate values for the total pressure loss and the combustor efficiency can be taken from [1].

With the outer diameter of the engine given, the basic combustor efficiency and total pressure loss, the turbine inlet temperature and an estimated HPT isentropic efficiency the thermodynamic considerations can be reduced to a trade-off between compressor efficiency and compressor total pressure ratio in order to achieve the best SFC for the engine.

Figure 2 depicts the SFC as a function of the total pressure ratio  $\Pi_{tc}$  over the compressor and the its isentropic efficiency  $\eta_c$ . The total pressure ratio was varied between 3 and 11 whereas the isentropic efficiency was gradually increased from 0.7 to 0.9. The colored contours show the thermodynamic cycle efficiency of the engine. The isentropic efficiency of the HPT and the PT were estimated at 0.87 and 0.88, respectively. The turbine inlet temperature was 1100K and the burner efficiency was set to 0.9. Furthermore, a burner pressure ratio of 0.9 was assumed.

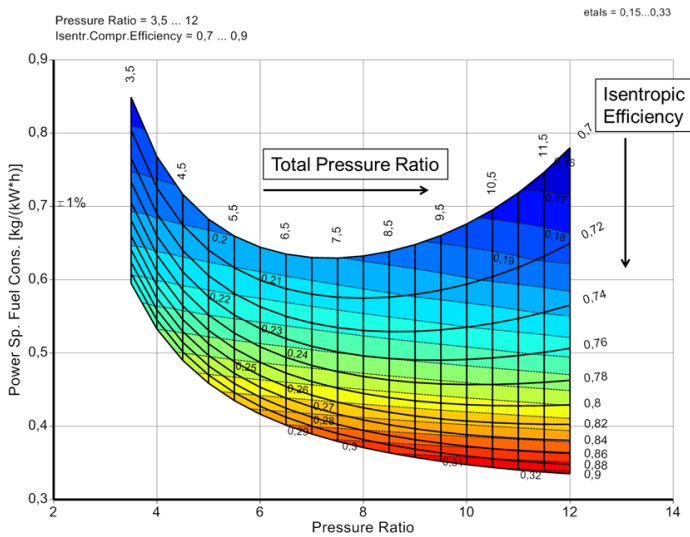


**FIGURE 2.** Specific fuel consumption [kg/(kW\*s)] depending on the total pressure ratio of the compressor and its isentropic efficiency. The colored contours show the thermodynamic cycle efficiency of the engine.

A few important conclusions can be drawn from figure 2:

- The SFC can be improved with a higher  $\eta_c$ .
- For every  $\eta_c$  there is an optimal  $\Pi_c$ .
- The total pressure ratio for the best SFC is higher than the total pressure ratio for the best cycle efficiency.
- At low compressor efficiency the partial derivative  $\frac{\partial SFC}{\partial \Pi_c}$  is steep.
- At higher compressor efficiency the partial derivative  $\frac{\partial SFC}{\partial \Pi_c}$  is flat.

At this point a trade-off has to be made between the flight envelope of the aircraft and the level of complexity of the compressor. A high  $\Pi_c$  and a high  $n_c$  leads to a very good SFC at ADP and the low power off design conditions such as Cruise at the cost of an expensive and complex compressor. On the other hand, a more simple and cheap compressor design, e.g. a single stage radial compressor results in intermediate SFC values. An interesting off design focused solution may also be a very high total pressure ratio and a rather low efficiency providing the best SFC values in off design (approx. same efficiency but lower total pressure ratio leads to enhanced SFC).

## COMPRESSOR CONCEPT

In order to get a good overview concerning the SFC values and the complexity of different compressor concepts, a decision matrix was created estimating the  $\Pi_c$ , the  $\eta_c$  and the complexity of different compressor concepts. The decision matrix is presented in table 2. Six compressor concepts have been assessed in the context of the very small engine diameter and combined with the results from figure 2.

The evaluation of the compressor concepts regarding their SFC values are shown in figure 3. The cell colors of the compressor concept in the table match the cell colors of the squares in figure 3.

The single stage radial compressor concept is the most common one in the given engine class. The advantages are the low engine integration complexity and the market availability of aerodynamically sound radial impellers. However, from an aerodynamic perspective, the design of the guide vane system at the impeller outlet is a very challenging task due to the high inlet Mach number and the deflection needed. Finally, the SFC was not expected to be lower than 0.7 kg/(kW\*h).

The biggest advantage of the two stage radial configuration is the high pressure ratio at the cost of a very challenging aerodynamic design process and a rather low efficiency. The overall SFC is not significantly enhanced in comparison to the single stage configuration. But, whereas the single stage configuration suffers from a significantly increased SFC at under speed off-design conditions (lower total pressure, nearly same efficiency), the SFC can even be even lower at under speed off-design conditions in the two stage radial concept.

The two stage concept combining an axial stage with a radial stage can deliver a intermediate  $\Pi_c$  and  $\eta_c$  in comparison to the

	Configuration	Est. $\Pi_c$	Est. $\eta_c$	Comp. Bladings	Comp. Duct	Comp. Manufactural Design
1	RAD	3.5-4.5	0.75	high	high	low
2	RAD-RAD	8-9	0.65-0.7	very high	very high	intermediate
3	AX-RAD	5.5-6.5	0.75-0.78	high	high	intermediate
4	AX-AX-AX	3.5	0.85-0.89	high	low	intermediate
5	AX-DIAG	4.5-5	0.85-0.87	high	low	high
6	AX-AX-DIAG	6-6.5	0.83-0.85	very high	intermediate	high

**TABLE 2.** Decision matrix of different compressor concepts. RAD: radial stage AX: axial stage DIAG: mixed flow stage

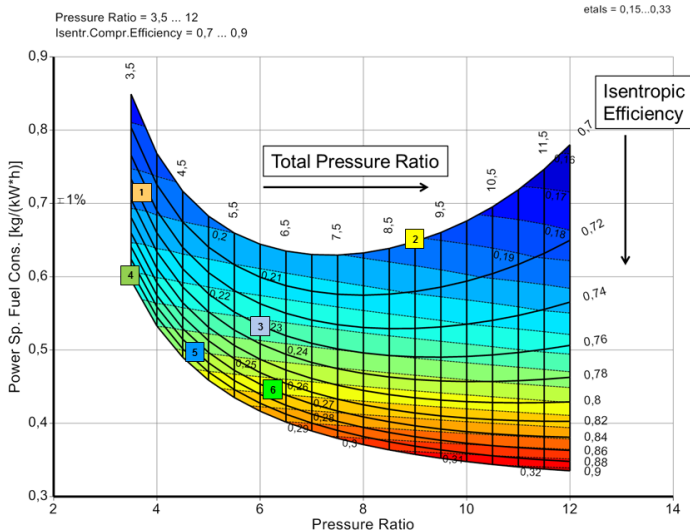


**FIGURE 3.** Specific fuel consumption [kg/(kW\*s)] depending on the compressor total pressure ratio and compressor isentropic efficiency. The colored contours show the thermodynamic cycle efficiency of the engine. The colored squares mark the different compressor concepts from table 2.

other concepts, leading to an intermediate SFC value. However, the aerodynamical matching between a full axial stage and a radial stage requires a tuning of the blade tip speeds and thus the blade loading of both stages. Furthermore, the estimated  $n_c$  of 0.75-0.78 still does not have favorable effects on the off-design SFC behavior.

The three axial stages compressor concept provides the highest estimated efficiency but the lowest total pressure ratio. Thus, the SFC at e.g. Cruise conditions is an important drawback of this concept.

Finally, two axial-mixed flow stage concepts are discussed. A mixed flow stage is able to provide a high total pressure ratio and a relatively high efficiency combined with an increased mass flow density [2]. The real aerodynamical challenge of this concept is nevertheless the design of the stator of the diagonal

stage. The stator design has to provide a very high flow turning at a high inlet Mach number. At the same time, the stator system must decrease the meridional Mach number to values around 0.2 in order to minimize the total pressure loss over the burner.

AeroDesignWorks estimated that the axial-diagonal concepts outclass the other concepts in terms of ADP SFC and off-design sensitivity of the SFC. The three stage axial-axial-diagonal concept was finally selected as it provides the best estimated SFC values at the cost of a very challenging aerodynamic design and a comparatively high engine integration complexity.

## DESIGN PHILOSOPHY

To describe the full pathway to the aero-mechanical design of the three stage axial-axial-diagonal compressor is beyond the scope of this paper. A similar parameterization approach was used for the airfoil design as presented in the second part of this paper, which deals with design and automated optimization of the turbines stages [3]. Following a preliminary design phase, the design was completed via multi-objective, multi-disciplinary 3D automated optimization. However, much of the flow path design and the stage loading distribution was done manually seeking to decrease the number of degrees of freedom of the optimization process. All numerical simulations were conducted with the DLR flow solver TRACE [4, 5].

The optimization process was performed by use of the DLR optimization framework AutoOpti [6, 7, 8]. The aero-mechanical optimization included up to four aerodynamic operating points at design speed and about 80% of the design speed. The mechanical part included a static stress analysis of the blades and a modal frequency analysis and tuning with a fixed blade hub approach. Furthermore, a hot-to-cold iterative calculation process was used to conduct the static stress analysis and the modal frequency analysis, starting from the proper cold geometry.

## COMPRESSOR GEOMETRY

The full compressor geometry as well as a meridional view are shown in figure 4. The design includes two axial stages

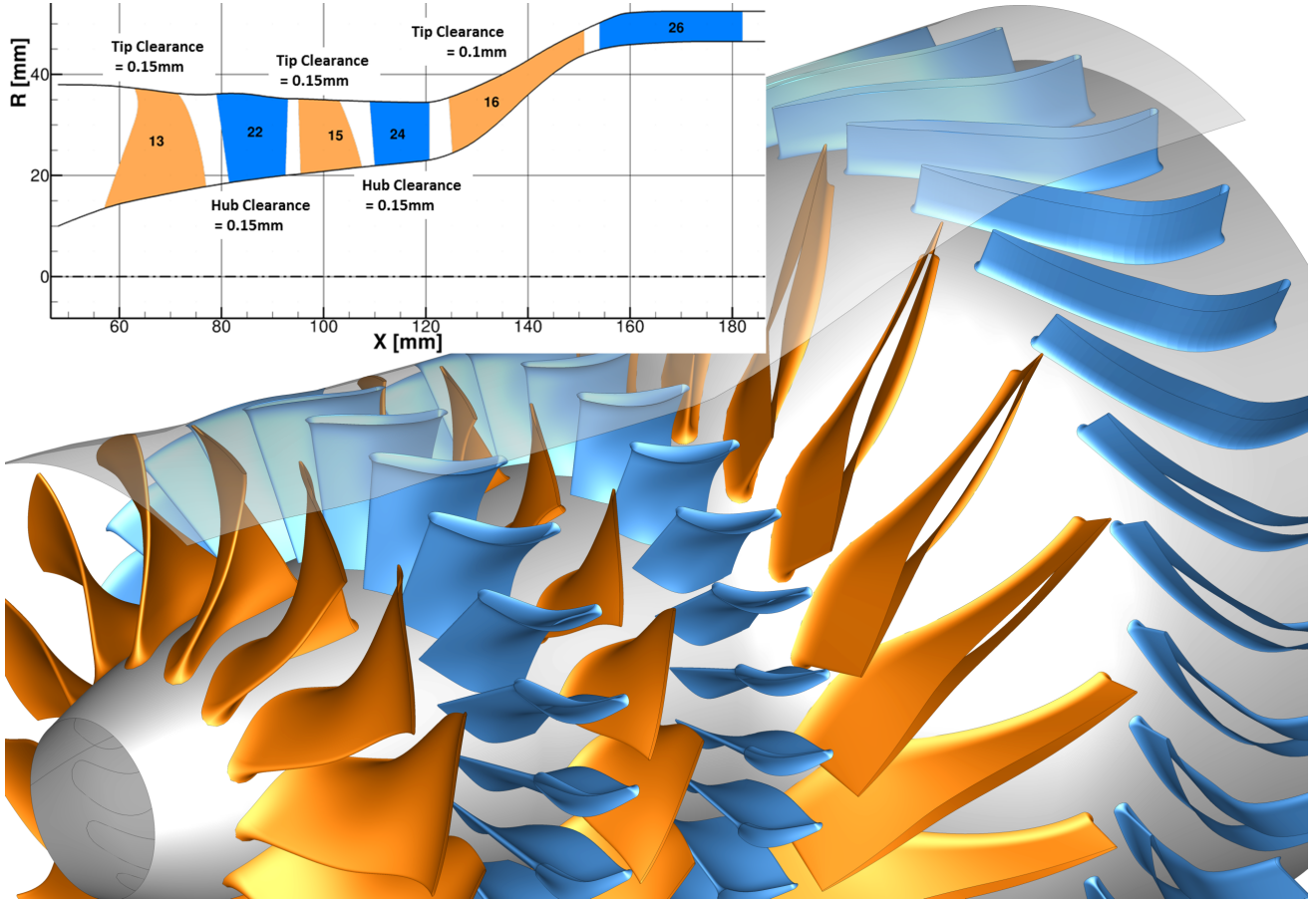


**FIGURE 4.** 3D compressor geometry and meridional view

and one mixed-flow stage. The axial stators are designed as cantilevered stators. The stator of the diagonal stage is a fully shrouded design. It will contain the aft bearings and the 360°-machined full annulus part is inlaid in the casing half-shells.

The hub annulus line imposes a notable flow path contraction to the stages one and two. The contraction is split up between the rotor and the stator rows to reduce the loading of the stators in the area close to the inner end wall. The casing annulus line barely reaches 40mm of radius in front of the first rotor and imposes a slight contraction to the flow field up to stator 2. A small curvature of the outer duct is introduced at rotor I LE to reduce the streamline curvature in this sensible area. The rather flat casing annulus line shape in the diagonal rotor area mitigates the risk of a great interaction of local S2 curvature effects and the blade to blade airfoil section aerodynamics. The maximum outer annulus is about 55mm. The inner annulus line in the diagonal rotor area defines the relative inlet Mach number and also partially the inlet angle for the diagonal stage stator hub section being - the most critical section of the stator design.

As seen in figure 4, the diagonal stator cannot profit from any flow duct contraction as the meridional Mach number has to be reduced to values of about 0.2.

Table 3 presents the blade count and the estimated “hot” clearance heights for each blade row.

	Blade count [-]	Clearance height [mm]
Rotor I	13	0.15
Stator I	22	0.15
Rotor II	15	0.15
Stator II	24	0.15
Rotor III	16	0.1
Stator III	26	-

**TABLE 3.** Blade counts and hot clearance heights of the compressor

## THE COMPRESSOR PERFORMANCE MAP

The numerical compressor performance map is presented in figure 5. The bottom frame shows the full performance map in terms of  $\Pi_c$  over the compressor massflow. Rotating speeds between 35% and 102.5% of the design speed have been simulated and assessed. The design goal of a total pressure ratio of about 6.25 on the working line was achieved. The compressor design ensures about 20% surge margin (SM) relative to the chosen working line throughout the whole compressor map. The upper frame depicts the zoomed performance map of the primary operating area of the compressor in terms of  $\eta_c$  over the massflow.

Numerically, isentropic efficiency values of about 81% were achieved on the working line between 89% and 90% of the nominal speed which is about 2% lower than the initial estimate in table 2. The efficiency effects of this small scale compressor have been underestimated. Nevertheless, a well matched three stage axial-axial-diagonal compressor has been designed with reasonable total pressure ratio, isentropic efficiency and surge margin over the full operating range.

Furthermore, it can be expected that a simple scale up of the engine, e.g. 2:1, will notably increase the isentropic efficiency of the compressor due to relatively lower clearance loss and wall friction losses.

## STAGE LOADING AT ADP CONDITIONS

The operating point ADP refers to design speed conditions on the working line. The operating point is shown in the performance map as black circle in the bottom frame of figure 5. A summary of the overall performance data at ADP conditions is also shown in table 4. Isentropic efficiency values are also given. The first and second stage provide a stage pressure ratio of 1.54 and 1.44, respectively. The total pressure ratio of the third stage is 2.79. The first two stages of the compressor are choked at ADP conditions to guarantee a reasonable SM, pushing the isentropic efficiency to quite low 76%. A meridional view of the meridional Mach number distribution and the total pressure distribution throughout the compressor are shown in figure 6.

	$\Pi_t$	$\Pi_s$	$\eta$
Compressor	6.2	6.8	0.76
Stage I	1.54	1.48	0.796
Stage II	1.44	1.46	0.811
Stage III	2.79	3.15	0.781

TABLE 4. Compressor and stage loading overview

The meridional inflow Mach number at about 50% relative

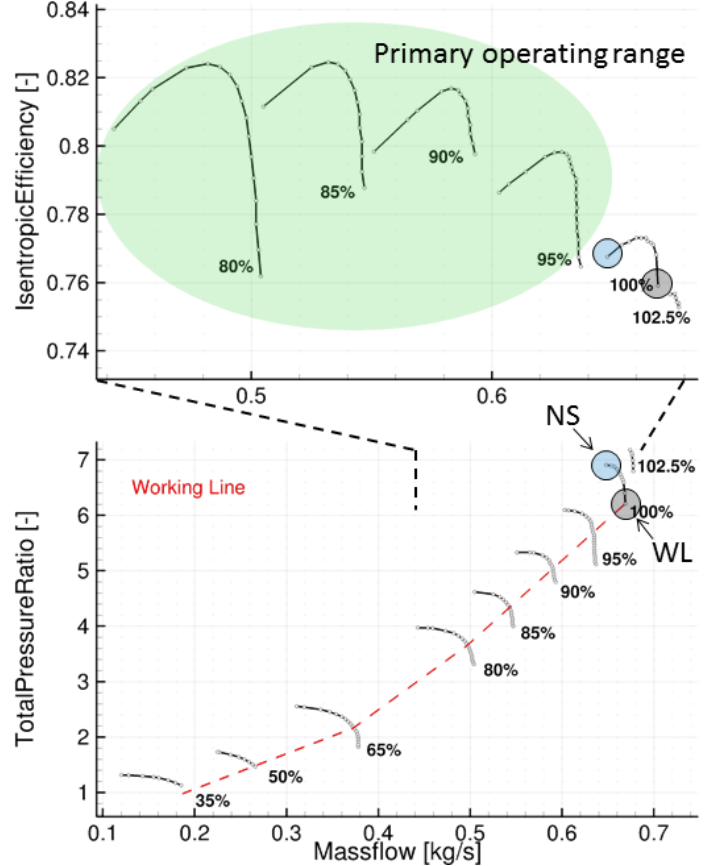


FIGURE 5. Numerical compressor performance map:

- full performance map  $\Pi_c$  over mass flow (bottom frame)
  - zoomed performance map of the primary operating area,  $\eta_c$  over massflow (top frame)
- Working line (WL) and near stall (NS) operating points at design speed are shown by black and blue circles.

span is about 0.55 and is maintained to the stator II outlet plane. The relatively high meridional Mach number at the stator II outlet plane leads to a very high meridional Mach number at the rotor III outlet plane. This eventually results in an extremely high aerodynamic loading of stator III and consequently to high total pressure losses as shown in the lower frame of figure 6.

Thus, aiming to improve the datum design further, one could focus on the reduction of the meridional Mach number throughout the two axial stages in order to reduce the stator III loading.

Finally, a number of interesting technology based parameters is given in table 5. The engine runs at 105000 rounds per minute and provides a massflow to area ratio of 158.8 kg/(s\*m<sup>2</sup>) at the compressor inlet.  $\Phi_{Utip}$  and  $\Psi_{Utip}$  refer to the flow ( $\Phi = \frac{C_m}{U}$ ) and loading ( $\Psi = \frac{2\Delta h}{U^2}$ ) coefficients, respectively, with reference to the rotor tip speed  $Utip$ . In contrast to the

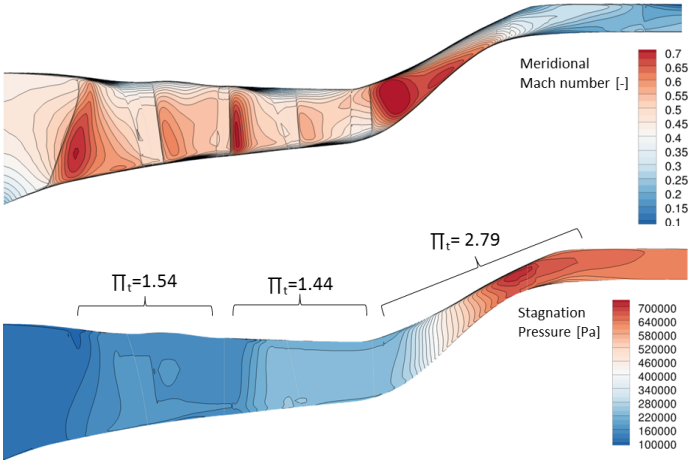


**FIGURE 6.** Meridional view of  
a) Meridional Mach number distribution (top frame)  
b) Total pressure distribution (bottom frame)

latter  $\Psi_{Uaverage}$  defines the loading coefficient with reference to the massflow averaged circumferential speed  $Uaverage$ . Furthermore, the reaction degree in terms of enthalpy is shown in table 5.

	Stage I	Stage II	Stage III
RPM [1/min]	105000	105000	105000
$\Phi_{Utip}[-]$	0.355	0.463	0.333
$\Psi_{Utip}[-]$	0.615	0.629	1.128
$\Psi_{Uaverage}[-]$	0.644	0.627	1.003
Reaction Enthalpy [-]	0.755	0.763	0.665
Massflow per $m^2$ [ $kg/(s \cdot m^2)$ ]	158.8	-	-

**TABLE 5.** Technology parameters of stages

## STAGE AERODYNAMICS: WORKING LINE VERSUS NEAR STALL

This chapter aims to analyze the aerodynamics of the three stages in more detail. Even though it is beyond the scope of this work to show the aerodynamics of each stage over the full operating range, a detailed view of the aerodynamics at nominal speed might give a better understanding of the engine. Both operating points to be considered, WL and NS are depicted by the black and blue circle symbols in figure 5, respectively.

The overall  $\Pi_t$  rises from about 6.2 at WL (choke) conditions to about 7 at NS conditions. The compressor isentropic efficiency raises from about 76% at WL to about 77% at NS. The maximum efficiency operating point is numerically calculated to 77.5%.

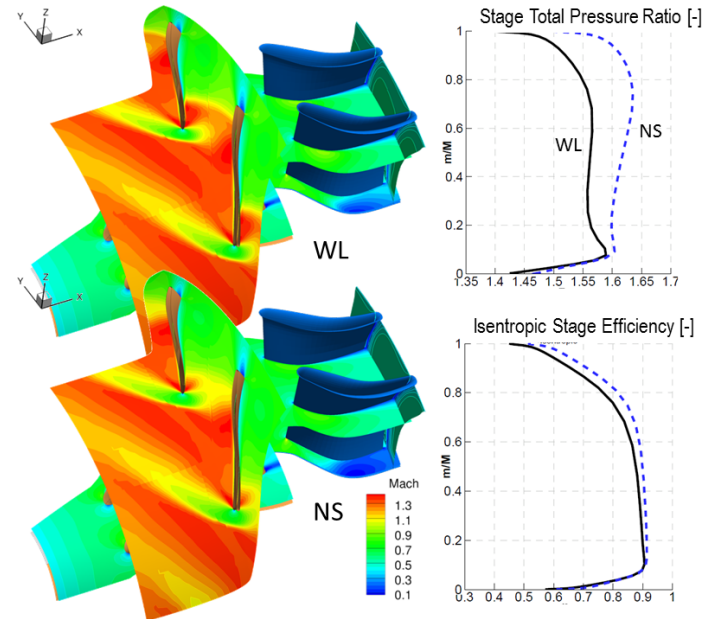


**FIGURE 7.** Stage I:  
a) Iso-contours of the Mach number in the relative reference frame close to blade hub and tip at WL and NS conditions  
b) Radial distribution of the relative massflow  $m/M$  over the isentropic stage efficiency and the stage total pressure ratio. WL conditions are marked by the black solid line, NS conditions by the dotted blue line.

Figure 7 shows an overview of the aerodynamics of the first stage. The top frame shows the comparison of the relative Mach number in a blade-to-blade section close to the blade tip between the WL and the NS condition. At WL conditions the rotor I is choked close to the blade tip. At NS the shock system is pushed upstream and ends up in a massive LE bow shock system. At the stator side, the clearance losses can be clearly identified via the low Mach number area around the stator SS at the hub endwall.

The bottom frames of figure 7 depict the radial distribution of the isentropic efficiency and the total pressure ratio of the first compressor stage. The clearance and end wall losses have a notable impact on the overall stage performance. Especially the stator clearance losses can be clearly identified. The overall stage pressure ratio is increased to 1.6 at NS conditions, showing the typical loading shift from a radial equally balanced loading at WL conditions to more tip loaded design at NS conditions.

Figure 8 provides the same picture setup as figure 7 for the

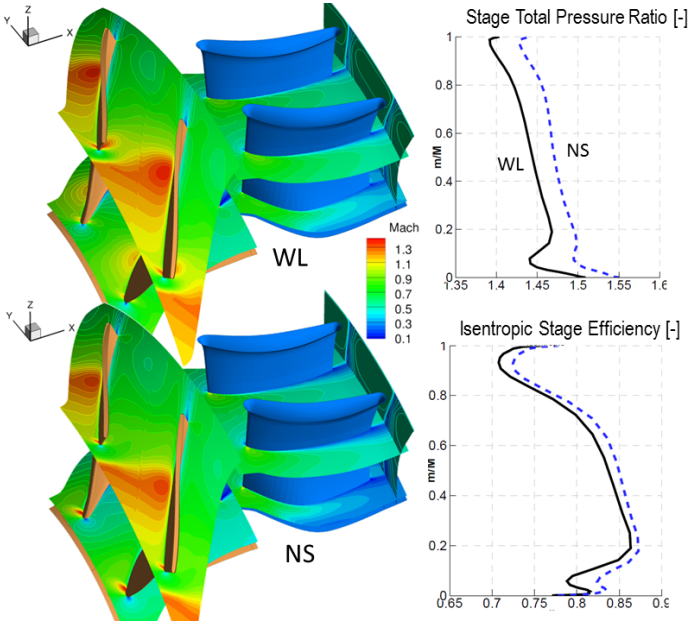


**FIGURE 8.** Stage II:

a) Iso contours of the Mach number in the relative reference frame close to blade hub and tip at WL and NS conditions  
b) Radial distribution of the relative massflow  $m/M$  over the isentropic stage efficiency and the stage total pressure ratio. WL conditions are marked by the black solid line, NS conditions by the dotted blue line.

second axial stage. The second rotor is only slightly choked at the blade to blade plane close to the blade tip. At NS conditions the shock system is close to the maximum efficiency state. Once more, the stator hub clearance losses are well captured by the iso-Mach contours of stator II. Regarding the radial total pressure distribution of the stage, it has to be mentioned that a total pressure ratio increase is achieved over the full duct span and that a radial load shift cannot be observed. Furthermore, it might be of interest that the second stage reaches its maximum isentropic stage efficiency of about 87% at about 85% nominal speed.

Finally, the the analogous set of pictures for the diagonal stage is presented in figure 9. Rotor III is clearly choked in the vicinity of the blade tip at WL conditions. Furthermore, the footprint of the tip clearance vortex can be identified via the low Mach number area at the blade's SS. The extremely high loading and massive diffusion of stator III result in a high total pressure loss and flow separation at the hub section. The total pressure ratio of stage III is increased from about 2.8 to about 3 from WL to NS conditions, with a minor increase in efficiency.

## STRUCTURAL BLADE MECHANICS

The material of the three compressor rotors is the titanium alloy “Ti 6Al 4V”, since it is planned to machine the whole

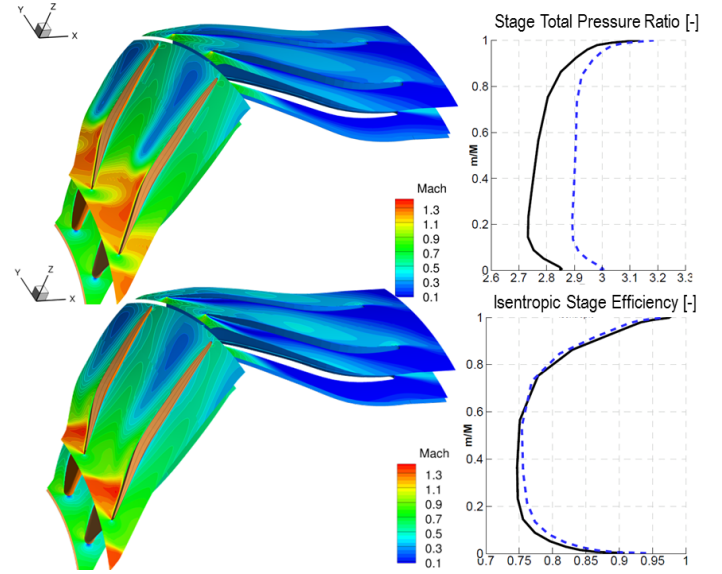


**FIGURE 9.** Stage III:

a) Iso contours of the Mach number in the relative reference frame close to blade hub and tip at WL and NS conditions  
b) Radial distribution of the relative massflow  $m/M$  over the isentropic stage efficiency and the stage total pressure ratio. WL conditions are marked by the black solid line, NS conditions by the dotted blue line.

rotating system as one single component and the third rotor does not allow for the use of a high-strength aluminium alloy, for temperature reasons. However, during optimization the first two rotors were assumed to be made of high-strength aluminium alloy “EN AW-7075” and the diagonal rotor III from the steel “T700”. Fortunately, the change of material to titanium had only very small effect on the relative material loading since the quotient of density to Young’s modulus is very similar for the aluminium and the titanium alloy. By the example of rotor I the mechanical properties are shown in figure 10. This blade is, in terms of mechanics, the most critical. Both other rotors II/III show much lower stress values. The maximum stress with a value of about 500Mpa (vonMises=447MPa) is located on the blade pressure side at the onset of the fillet. This seems to be acceptable since the centered location is more convenient than e.g. the root of the leading edge, which might endure higher dynamic loadings due to chord-wise blade vibrations.

The dynamic criteria were implemented as constraints in the optimization. Centering the first bending mode in between the 2nd and 3rd engine order and avoiding other crossings with lower engine orders was achieved without any problems. Due to the very stiff design of the disc, the dynamic results from calculations with/without disc provide very similar results. Also depicted in figure 10 is a comparison of the hot “parameterized” blade (red surface) and the iteratively computed “cold” geometry.

The integrated aero-mechanical optimization provided a feasible geometry for these highly-twisted and mechanically loaded blades, which required no further aero-mechanical iterations.

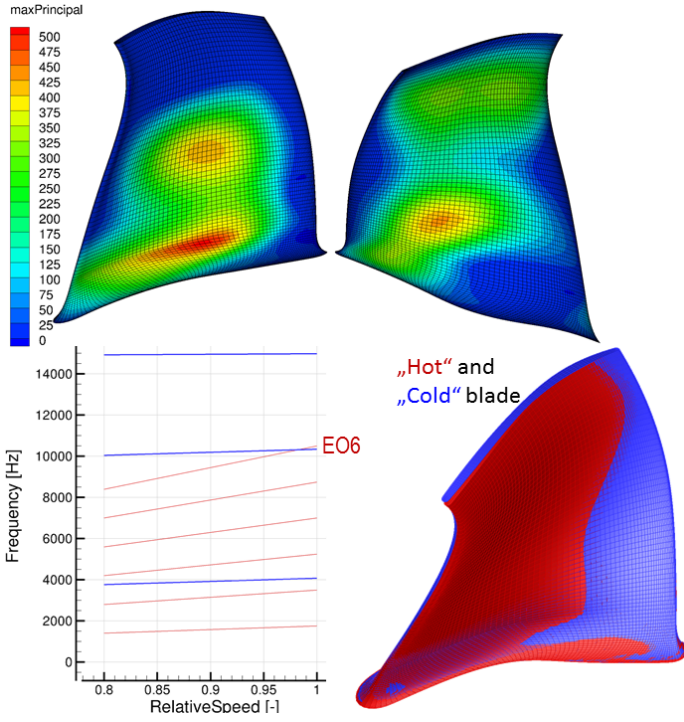


**FIGURE 10.** Structural Blade mechanics Rotor I:

- Iso contours of the static blade primary stress (top frame)
- Campbell-diagram of Rotor I with fixed hub boundary condition (bottom left frame)
- Geometrical difference of hot (red) and cold (blue) blade (bottom right frame)

## AEROELASTICITY: ROTOR I FLUTTER ASSESSMENT

While aeroelasticity was not part of the design optimization process, a flutter assessment of both axial rotor blades was conducted for the final configuration. From the steady-state CFD performance map calculations the bounding throttle points of the operating range were selected for the flutter analysis using a linearized approach in TRACE. The first three modes of both rotors were evaluated on the working line at  $n_{rel} = 0.8$  and  $n_{rel} = 1.0$  as well as for the last converged operating points close to numerical stall for the same rotational speeds. For each of the 12 cases (3 modes \* 4 operating points) the aerodynamic damping curve was resolved by steps of  $\Delta IBPA = 10^\circ$  of the inter-blade phase angle.

Figure 11 shows results of the rotor I at WL conditions for nominal rotational speed. All damping curves are positive,

hence blade flutter is not to be expected. The local aerodynamic work distribution in the lower graphs allow for physical interpretations. The first mode is the first bending mode (1F). The de-throttled shock-system at WL conditions in the tip region goes along with an aerodynamically unloaded leading edge, which is also insensitive to small angular changes of the blade. The subsonic rear part of the upper blade passage is responsible for local work input to the blade, decreasing the aerodynamic damping.

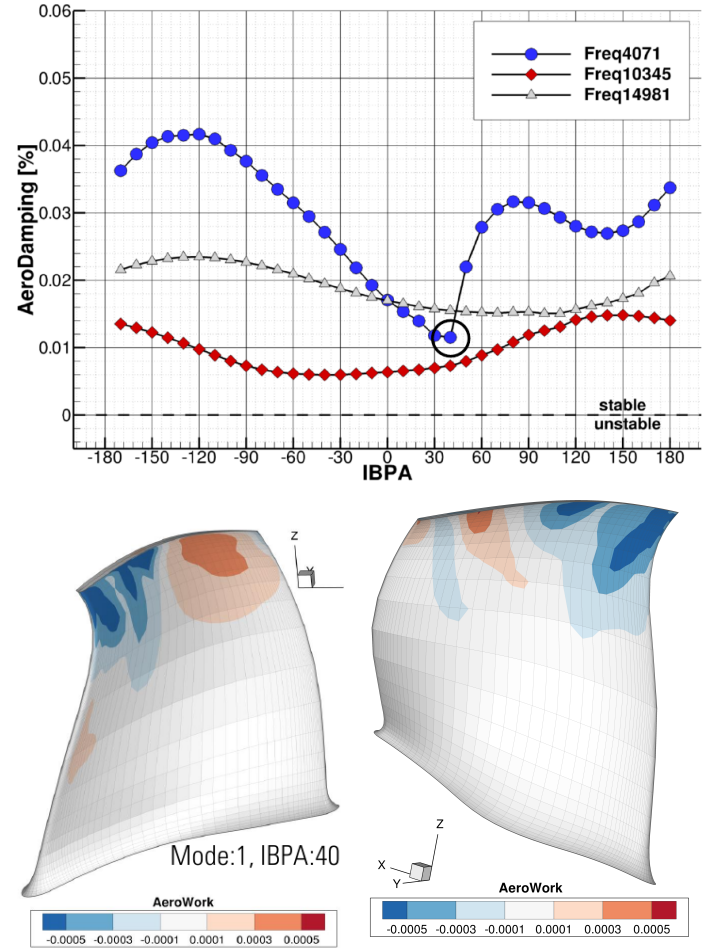


**FIGURE 11.** Rotor I, Mode 1, WL @  $n_{rel} = 1.0$ :

Aerodynamic damping curve at nominal speed WL conditions for the first three eigenmodes of rotor I with a 10 degree IBPA step width (upper frame) and iso-contours of the local aerodynamic work of the flow on the blade surface. Positive values mark local energy input to the blade.

The rotor I is stable with respect to fluttering even in near stall conditions at nominal speed. Figure 12 shows the same results as previously shown for the working line points but with

focus on the second mode at its minimum aerodynamic damping (IBPA=-10°). The second mode mixes the second bending and first torsion mode. The shock system close to stall is pushed further upstream, resulting in a more highly loaded leading edge region. Oscillation of the shock onset on the pressure side is triggered by this mode, resulting in a locally high work input to the blade at this location.

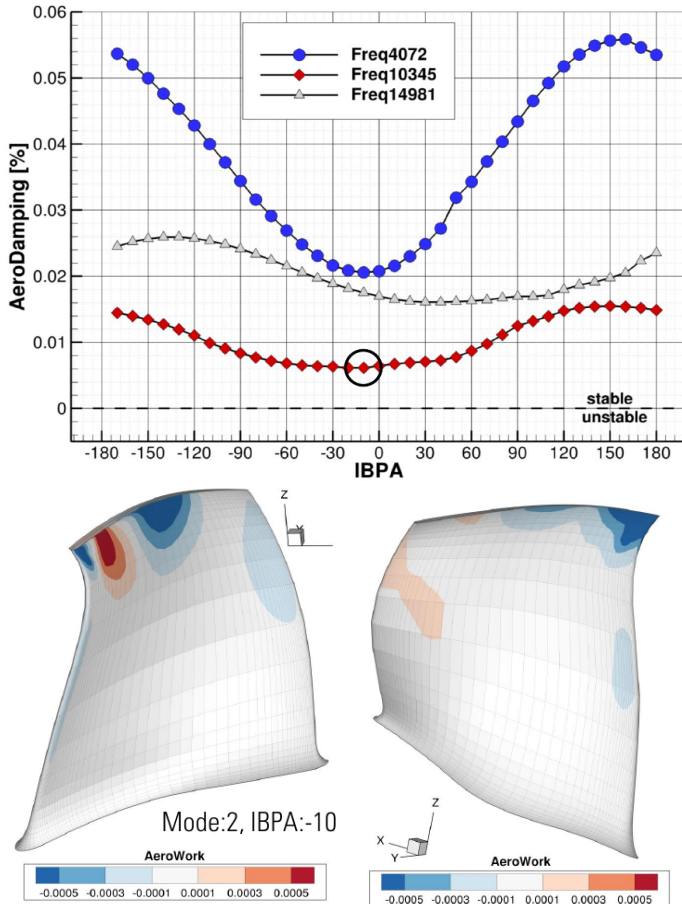


**FIGURE 12.** Rotor I, Mode 2, NS @  $n_{rel} = 1.0$ :  
Aerodynamic damping curve at nominal speed NS conditions for the first three eigenmodes of rotor I with a 10 degree IBPA step width (upper frame) and iso-contours of the local aerodynamic work of the flow on the blade surface. Positive values mark local energy input to the blade.

## CONCLUSION AND OUTLOOK

This paper deals with conceptual considerations and a three stage compressor design for a small scale turboshaft engine. In the first part the thermodynamic cycle is analyzed by the example of Swiss UAV's helicopter drone NEO S-350. For this purpose

several possible compressor concepts are evaluated in terms of achievable performance parameters and their effect on specific fuel burn as well as cost and manufactural aspects.

Due to its high flow density, high achievable efficiency and pressure ratio, a three stage compressor consisting of two axial front stages and a mixed-flow rear stage was selected as the most promising concept. In the last step of the same project, this compressor was designed by automated, multi-disciplinary optimization including several operating points and a structural mechanics assessment. An overview is given of the final compressor design and performance: The highly-loaded configuration provides an overall total pressure ratio of 6.2 with an adiabatic efficiency at nominal speed of 76%. Toward the SFC-critical operating points with lower rotational speed, the calculated efficiency exceeds 80%. These performance values are very reasonable for a compressor of this size with the large relative tip clearance sizes and edge thicknesses. However, there is some potential in lowering the meridional Mach number over the axial front stages and consequently lowering aerodynamic loading and losses of the last stator row.

Assessment of the static and dynamic rotor mechanics in the optimization campaign led to mature blade geometries regarding aerodynamics and mechanics, which passed all further evaluations for product use without changes. The aero-mechanical results were also used for a flutter stability assessment of the axial rotor blades in a very efficient manner, using a linearized 3D method - which was successfully passed as well.

In the next project phase the two-stage turbine system was designed as well, results from this work are presented in the second part of this paper. With all the design tasks successfully completed, a prototype test of the engine as well as a component rig-test of the compressor are expected in 2014.

## References

- [1] Hupfer, A., Erhard, W., and Kau, H.-P., 2012. "Investigation of combustor concepts for micro gas turbine jet engines". *23rd International Symposium on Transport Phenomena, Auckland, New Zealand*.
- [2] Mönig, R., 1990. "Entwicklung und Untersuchung eines diagonalen Überschallverdichter-Laufrads mit querschnittskontrollierter Stoßverzögerung". PhD thesis, RWTH Aachen.
- [3] Siller, U., Kröger, Moser, T., and Hediger, S., 2014. "Towards a highly efficient small scale turboshaft engine. part 2: Aero-mechanical turbine design and optimization.". *ASME Turbo Expo 2014, Düsseldorf, Germany GT2014-26320*.
- [4] Becker, K., Heitkamp, K., and Kügeler, E., Lisbon, Portugal, 2010. "Recent progress in a hybrid-grid cfd solver for turbomachinery flows". *Proceedings of V European*

*Conference on Computational Fluid Dynamics ECCOMAS CFD.*

- [5] Ashcroft, G., Heitkamp, K., and Kügeler, E., Lisbon, Portugal, 2010. “High-order accurate implicit runge-kutta schemes for the simulation of unsteady flow phenomena in turbomachinery”. *Proceedings of V European Conference on Computational Fluid Dynamics ECCOMAS CFD*.
- [6] Voß, C., Aulich, M., Kaplan, B., and Nicke, E., 2006. “Automated multiobjective optimization in axial compressor blade design”. *ASME Turbo Expo 2006, Barcelona, Spain GT2006-90420*.
- [7] Siller, U., Voß, C., and Nicke, E., 2009. “Automated Multidisciplinary Optimization of a Transonic Axial Compressor”. *47 th AIAA Aerospace Sciences Meeting, Orlando, USA, AIAA-2009-0863*.
- [8] Kröger, G., Voß, C., and Nicke, E., 2010. “Axisymmetric Casing Optimization for Transonic Compressor Rotors”. *ISROMAC 13 2010, Honolulu, USA, ISROMAC-2010-20010*.